Check for updates

Tensile properties of single- and multi-type mixed fibre bundles of spider silk

Siripanyo Promnil, [ID] *[a] Daniele Liprandi, [ID] [a] Tom Illing,[ab] Maitry Jani, [ID] [a] Paula Heinz [ID] [a] and Jonas O. Wolff [ID] [a]

Spider silk is known for its outstanding toughness at low density, making it a promising model for the biomimetic design of advanced fibre materials. Spiders naturally do not spin single silk fibres but instead produce bundles, or threads, composed of two or more fibres that may originate from the same or different silk glands. Despite their ubiquity, the mechanical properties of these fibre bundles have been largely overlooked. In this study, both naturally spun and forcibly silked fibre bundles from the cosmopolitan cellar spider *Pholcus phalangioides* (Pholcidae) and naturally spun bundles from the comb-footed cellar spider *Nesticus cellulanus* (Nesticidae) were examined to test whether post-spinning combinations of different silk materials, such as stiff and soft fibres, enhance the toughness of silk bundles. Despite their compositional diversity, tensile tests showed that the performance of fibre bundles cannot be predicted solely from the properties or the number of the individual fibres. These findings reveal that silk fibre bundles exhibit more complex tensile behaviour than previously recognised and demonstrate that spiders can produce a wide range of mechanical properties through the specific post-processing and combination of silk fibres. This principle of forming heterogeneous bundles may inspire biomimetic approaches to the post-spinning processing of recombinant silks and the design of advanced fibre materials.

Introduction

Spider silk is a remarkable natural material that has captivated scientists and researchers for decades due to its outstanding mechanical properties, combining high strength and toughness while being lightweight.[1] It is synthesised by silk glands and extruded through spigots on spinnerets, which are paired appendages at the end of the spider's abdomen.[2] Spider silk is primarily composed of large spidroins (spider silk proteins) that often contain highly repetitive sequences, some of which may form specific secondary structures, such as crystalline β-sheets.[3] The interplay between these hard crystalline domains and elastic semi-amorphous regions results in spider silk being both strong and elastic, and hence, remarkably tough.[4–6]

Spiders possess several types of silk glands, each producing a distinct type of silk with unique characteristics, based on different base spidroin compounds with different amino acid sequences.[7] The three main types of silk found in the majority of spiders are major ampullate silk, minor ampullate silk and aciniform silk. Major ampullate silk is the most studied type of spider silk. It is the main component of draglines and web frames, and is usually produced in the highest quantities of all silks by the spiders.[6] The properties and biological functions of minor ampullate and aciniform silk have only been studied in some orb-weaving spiders.[8,9] In the orb-weavers *Argiope* and *Larinioides*, for example, minor ampullate silk is less strong than major ampullate silk, and is used during web construction in single-use scaffolds, such as bridging lines and auxiliary spiral threads.[2,8,10,11] Aciniform silk is used in prey wraps and egg cases.[12] In *Argiope*, it was found to be the toughest of all silk types, which is largely attributed to the superior extensibility of aciniform fibres compared to other dry silks at similar strength.[11]

Natural spider silk materials frequently consist of a composite of materials or fibres originating from one or more types of silk glands. For example, draglines usually consist of two or four major ampullate fibres as they originate from paired spinnerets, each of which is equipped with the spigots (silk gland openings) of one or two major ampullate glands. In exceptionally large species, such as *Nephila pilipes*, the mooring threads of female spiders have been observed to contain 12.0 ± 5.0 fibres per thread.[13] In other species, it was observed that draglines typically comprise a mixture of two or more silk types: major ampullate and minor ampullate, sometimes with the addition of aciniform silk.[14] It is important to note that studies that characterised silk properties and composition were often based on major ampullate silk fibres that were forcibly pulled (silked) from the spinnerets of

[a] *Evolutionary Biomechanics, Zoological Institute and Museum, University of Greifswald, Loitzer Str. 26, 17489 Greifswald, Germany.*
E-mail: siripanyo.promnil@uni-greifswald.de
[b] *Institute of Physics, University of Greifswald, Felix-Hausdorff-Str. 6, 17489 Greifswald, Germany*

the immobilised spider.[15] If done carefully, forcible silking excludes any behavioural combination of silk fibre types that might naturally occur.

Other known examples of silk fibre composites that are naturally produced by spiders are the capture threads of orb webs, which may exhibit a mix of extensible fibres and viscid glue, or, as in the case of cribellar threads, a combination of different micro- and nano-fibres.[16–18] Cribellar threads usually contain two microfibre types, which are the reserve warps (also called undulating fibres, produced by the minor ampullate glands) and the axial fibres (produced by the pseudoflagelliform gland).[19–21] These microfibres are embedded in a mass of numerous convoluted nanofibres from the cribellar and paracribellar glands.[18,19,22] Gumfoot threads, on the other hand, are only partially glue-coated bundles of major and minor ampullate silk that occur in cobweb structures and are used to ensnare walking prey upon contact.[23,24] By strategically combining different silk types and leveraging the hierarchical structure and interactions at various length scales, spiders have evolved fibre bundles with optimised mechanical properties tailored for specific functions, such as web construction, prey capture, and structural support.[18]

Beyond major ampullate silk, our understanding of silk properties in non-orb weaving spiders remains limited, particularly on minor ampullate and aciniform silk[12] and threads from a combination thereof. Although multi-fibre silk threads have been mechanically tested in several orb-weaving spiders, these studies have primarily examined bundles composed of a single silk type, for example, major ampullate silk. These examples do not involve behaviourally assembled mixtures of different silk materials. In contrast, many non-orb-weaving spiders, including *Pholcus phalangioides* and *Nesticus cellulanus*, routinely spin threads that integrate two or more silk types within the same bundle, often in behaviour-specific contexts. The mechanical consequences of such naturally mixed-fibre bundles have not been systematically investigated – a gap we aim to close with this work.

The mechanical properties of fibre bundles are the product of both the combined tensile properties of the included fibre materials and the interactions between the individual fibres within the bundle (friction and adhesion).[16,18,25,26] In some bundles, a single material may govern the bundle properties. Other bundles exhibit more complex and less predictable tensile behaviours, *e.g.* due to some components exhibiting initial hidden lengths.[18] Insufficient knowledge of the mechanical properties of fibre bundles composed of multiple silk types limits our understanding of how spiders naturally use silks in natural functional contexts and restricts the potential for the development of bioengineered silk materials based on post-spinning fibre combinations.

The first aim of this study was to elucidate the mechanical properties of major ampullate, minor ampullate, and aciniform silk in a non-orb weaver spider, the cosmopolitan cellar spider *Pholcus phalangioides* (Synspermiata: Pholcidae). This species presents an intriguing case study, as our previous research has found that these three silk types are often used in varied

combinations in draglines, web building and prey wrapping.[27] This offers the opportunity to study the effect of post-spinning silk-type mixture in spider silk threads.

P. phalangioides produces several silk types with different behavioural roles and mechanical requirements: drop-down draglines provide strong support during descent and are typically composed of major and minor ampullate silk; walking draglines balance flexibility with durability during locomotion and can include all three silk types; bridging lines are single-use lines used for dispersal that only contain minor ampullate silk; and gumfoot threads act as spring-loaded, adhesive capture lines including a larger number of fibres than the draglines.[27] As these threads are spun under different conditions, differences in fibre structure and tensile performance are expected. For example, bridging lines are extracted very quickly with forceful movements of the legs[27] and gumfoot threads are constructed at low speeds.[28] Such spinning speeds may affect the diameter and nano-crystal alignments inside the fibres.[29,30] Building on this foundation, the present study extends the mechanical characterisation of *P. phalangioides* silk threads to include gumfoot threads and forcibly silked fibre bundles composed of major ampullate and aciniform fibres, to clarify how the mechanical properties of single-type and multi-type mixed fibre bundles differ from those of single silk fibres. In addition, to exclude that our findings were merely species-specific, we examined silk fibre bundles from *Nesticus cellulanus* (Araneoidea: Nesticidae), a species from a distinct evolutionary lineage that constructs a similar web architecture with gumfoot threads.

Materials and methods

Silk sample collection

A total of 35 adult *Pholcus phalangioides* spiders were collected from the greenhouses of the Old Botanical Garden of the University of Greifswald, from university buildings, and from nearby residential buildings in Greifswald. In addition, 7 adult *Nesticus cellulanus* spiders were collected from Baden-Württemberg, Germany. The *P. phalangioides* were housed at 20–26 °C and ~70% relative humidity in plastic containers inside a climate chamber. *Nesticus cellulanus* were housed separately under cooler conditions of 11–13 °C and ~70% relative humidity in a beverage fridge. The spiders were weekly fed with house flies or fruit flies, and moisture was provided by spraying water into the containers or onto cotton balls placed inside. Spider silk threads were collected on black cardboard frames[11,31,32] containing three square holes (11 mm × 11 mm), each lined with double-sided adhesive tape to secure the threads. This design allowed three replicates of each sample to be prepared for different analyses. Prior to usage, the cardboard frames were reversibly attached to glass microscope slides using photo tape for stability during storage, handling, and imaging. The photo tape was weak enough to allow the cardboard frames to be removed easily from the slides before tensile testing.[27] Different silk threads were collected using
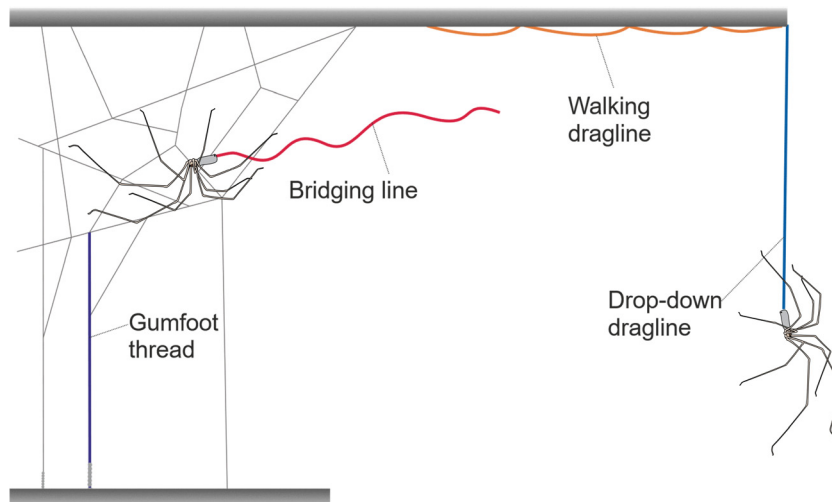
Fig. 1 Spider silks from the behaviours observed. In violet, gumfoot. In red, bridging line. In orange, walking dragline. In blue, drop-down dragline.

specific methods. Drop-down dragline silk was obtained by allowing the spider to descend from a lab stand at its natural spinning rate, and the silk thread was collected on the sample holder from above the descending spider. The collection of walking draglines and bridging lines followed the protocol described by Jani (2025).[27] Gumfoot capture threads are vertical lines attached to the bottom of the container with a viscid adhesive mass at the bottom end. Sections of these threads (above the viscid mass) were collected by placing the sample holder vertically and moving it closer until the thread adhered to the sample holder. Excessive thread (from the above tangle) was cut off. The different thread types are illustrated in Fig. 1.

Aciniform fibres and posterior median spinneret (PMS) fibres (minor ampullate with adhered aciniform silk) were collected by forcible silking. For this, the spiders were anaesthetised with CO_2 and restrained on a small Styrofoam platform with thin strips of masking tape. Under a stereomicroscope, the spigots of the posterior median spinnerets were observed, with each spinneret possessing one minor ampullate and one aciniform gland spigot. Aciniform spigots are identifiable as the smallest spigots with a cylindrical tip. Single aciniform fibres were extracted by carefully approaching the spinneret using a custom-made tool. This tool was prepared by attaching an insect pin (tip radius 0.20 mm) to the tip of a glass pipette. The tip of the pin was gently abraded on the surface to create a small curvature, which helped the fibre remain attached to the pin during extraction. In some cases where fibre extraction was difficult, the fourth leg of a dead specimen of *P. phalangioides* was mounted on a toothpick and rubbed gently over the spinnerets to help release the fibres. However, this method was not consistently successful, and the reason for fibre release remained ambiguous and random. Once a fibre became attached to the probe, it was pulled from the spigot at a slow and steady pulling speed of approximately 1 mm s^{-1}. This speed was achieved through repeated practice to standardise hand movement, as motorised reeling was not feasible for these small spiders and small distances. Only short strands of silk

could be extracted, as even slight mechanical vibrations caused premature fibre breakage and resulted in inconsistent or unusable threads. Although minor variation in hand-driven pulling speed is unavoidable, repeated trial collections confirmed that the produced fibres were of consistent diameter and morphology. The extracted fibres were subsequently mounted on single 11 mm × 11 mm cardboard frames. For PMS fibre bundles, all fibres originating from the posterior median spinnerets (*i.e.*, both minor ampullate and aciniform) were jointly pulled out and mounted on cardboard frames and secured it on glass slides. Isolated minor ampullate fibres could not be extracted. Also, trials to forcibly silk major ampullate silk from *P. phalangioides* remained unsuccessful.

Before the tensile tests, silk samples were secured with water-based white liquid glue along the edges of the cardboard frame (fixing the gauge length of the mounted fibre sample), and a small piece of paper was placed on top of the remaining double-sided sticky tape to prevent adherence to the nano-tensile machine clamps.

Microscopy

We utilised an inverted polarised transmission light microscope (AXIO Vert.A1, Carl Zeiss Microscopy Deutschland GmbH, Oberkochen, Germany) to examine the number of fibres within each silk thread sample.[33] Using the ZEN3.7 software, we measured the diameter of these fibres, obtaining 5–10 diameter values in different places of the same fibre type and subsequently calculating the average value per thread.

For additional information on the fine structure of different silk threads, we mounted a selection of naturally spun thread samples onto aluminium stubs with double-sided adhesive carbon tape. The samples were sputter-coated with Au–Pd (ratio: 80/20; polaron SC7640) and viewed in a scanning electron microscope (SEM) (Zeiss EVO LS 10, Carl Zeiss, Oberkochen, Germany) and field emission scanning electron microscopy (FE-SEM) (Zeiss Supra 40VP, Carl Zeiss, Oberkochen, Germany). Additionally, to examine fibre morphology

before and after mechanical deformation, we stretched selected dragline and gumfoot bundles to defined strain levels of 0.10, 0.30, and 0.40 mm mm^{-1} and imaged them using field emission scanning electron microscopy (FE-SEM).

For *Pholcus phalangioides*, sample size varied among silk types: two-fibre draglines were measured from two samples (taken from two spiders), four-fibre draglines from three samples (taken from three spiders), walking draglines from eleven samples (taken from five spiders), bridging lines from seven samples (taken from four spiders), and gumfoot threads from six samples (taken from three spiders). For *Nesticus cellulanus*, two-fibre draglines were measured from two samples (taken from two spiders), while four-fibre draglines, walking draglines, and gumfoot threads were each measured from one sample (taken from one spider). In this study, a sample refers to a single silk bundle segment mounted for mechanical testing or SEM imaging. Different silk samples collected from the same spider were treated as independent samples. All fibre diameter measurements for the morphology analysis were obtained from scanning electron micrographs. For each sample, fibre diameters were measured at several positions along the same fibre type, and the values were then averaged. The reported standard deviations, therefore, represent variation among measurements of the same silk type from different individuals and locations within each bundle.

Characterisation of mechanical properties

We utilised the T150 Universal Testing Machine (KLA, Milpitas, California, USA) to record force-extension data. Tensile tests were conducted at a constant extension rate of 1% strain per second until the fibre reached its breaking point, with a load resolution of 50 mN and extension resolution of 35 nm. Details of the testing procedure followed Blackledge and Hayashi.[11] The combined cross-sectional area used for the calculations of engineering stress was determined based on the number and average diameter of each fibre type present in the thread. The effective bundle cross-section area was calculated as $A_{\text{bundle}} = \sum_i \pi(d_i/2)^2$, where i indicates the different fibres in the bundle, and d is the fibre diameter.

All experiments were conducted under controlled environmental lab conditions (21.1–22.8 °C; relative humidity 30–40%). The calculation of engineering stress–strain curves and tensile properties such as stress at break (ultimate engineering strength), strain at break (ultimate engineering strain, or extensibility), Young's modulus, and toughness was performed using the KLA NanoSuite software.

Weibull distribution analysis

The variability in silk bundle strength was analysed using classical fracture mechanics principles. Following the weakest-link theory for fibrous materials, the failure strength of silk bundles was assumed to follow a two-parameter Weibull distribution:

$$P(\sigma) = 1 - \exp\left(-G \cdot \left(\frac{\sigma}{\sigma_0}\right)^m\right) \tag{1}$$

where $P(\sigma)$ represents the cumulative failure probability at stress σ, G is the geometrical parameter, m is the shape parameter indicating the repeatability of strength values, and σ_0 is the scale parameter representing the characteristic strength. To account for size-dependent effects, a modified Weibull distribution was employed:

$$P(\sigma) = 1 - \exp\left(-\left(\frac{G}{G_0}\right)^v \cdot \left(\frac{\sigma}{\sigma_0}\right)^m\right) \tag{2}$$

where G represents the cross-sectional area of the bundle, G_0 is the reference area (set to unity), and v is the size effect parameter. The Weibull parameters were determined using both linear regression and maximum likelihood methods on the linearised form of the distribution.

A goodness-of-fit test was performed for each silk bundle type, using $\alpha = 0.05$. Calculations and tests were performed using Python (version 3.12) and the Scipy[34] library.

Fracture mechanics analysis

The relationship between bundle strength and geometrical parameters was investigated using Griffith's criterion for elastic fracture. According to this criterion, the fracture stress scales as:

$$\sigma_{\text{f}} = \sqrt{\frac{\gamma E}{D}} \tag{3}$$

where γ is the strain energy release rate, E is the elastic modulus, and D is the equivalent fibre diameter calculated as $d = 2\sqrt{A/\pi}$, with A being the total cross-sectional area. Linear regression analysis was performed to evaluate correlations between strength and both $\sqrt{E/d}$ and $\sqrt{1/d}$, with statistical significance assessed using p-values (using $\alpha = 0.05$) and coefficients of determination. Calculations and tests were performed using Python (version 3.12) and the Scipy[34] library.

Finite element modelling

A linear elastic finite element method (FEM) analysis was conducted to investigate the mechanical behaviour of multi-fibre bundles under tensile loading. We considered different bundle geometries to verify the stress concentrations in different contact scenarios between fibres and considering partial fracture of the fibres in the bundle. The simulations were run using the linear elastic solver for solids provided by the library and the FEM environment MOFEM.[35] More details on this approach are provided in the SI.

Statistical analysis

Individual specimen variability was assessed by calculating relative standard deviations for mechanical properties both within individual spiders and across the entire population. Cross-sectional area measurements were correlated with strength values using logarithmic regression to determine size-effect relationships. All statistical analyses were performed with significance levels set at $\alpha = 0.05$, and correlations were evaluated using Pearson correlation coefficients. One-way analysis of variance (ANOVA) was conducted to compare the

individual tensile properties, including stress at break, strain at break, Young's modulus, and toughness, among seven types of silk threads for *P. phalangioides* and four types of silk threads for *N. cellanus*, corresponding to all the different varieties of silk bundles and single-silk fibres we were able to obtain from both species. *Post-hoc* Tukey's HSD tests were performed to test for pairwise differences after positive ANOVA analysis results.

Results

Morphology of *Pholcus phalangioides* silk threads

Scanning electron micrographs of naturally spun threads confirmed that *P. phalangioides* spiders produce threads composed of multiple fibres. As reported in previous works, walking draglines contained four to six fibres,[27] whereas gumfoot threads consisted of six to eight fibres.[24] In contrast, bridging lines consistently contained only two fibres per bundle.[27] The ultrastructural analysis of the silk bundles showed that the fibres run in a quasi-parallel way, without showing excessive roughness, knots or any other topological features (Fig. 2).

To identify which fibre types were present in each bundle, we referred to the fibre diameter ranges for each silk type as reported by Jani *et al.*[27] The proposed bundle compositions were inferred from the relative diameter differences between fibres observed in our SEM measurements. The two-fibre (N2) dragline (Fig. 2A) is likely composed of major or minor ampullate silk (diameter 0.947 ± 0.201 µm), whereas the four-fibre (N4) dragline (Fig. 2B) may consist of two major (diameter 0.433 ± 0.018 µm) and two minor ampullate fibres (diameter 0.760 ± 0.112 µm). Occasionally, aciniform fibres (diameter 0.276 ± 0.039 µm) were additionally present (N6). Walking draglines (Fig. 2C) may include two minor ampullate (diameter 1.078 ± 0.027 µm), two major ampullate (diameter 0.380 ± 0.029 µm), and up to two aciniform fibres in the six-fibre configuration, while the four-fibre configuration may consist of minor ampullate and aciniform fibres. Bridging lines (Fig. 2D), by contrast, appeared to contain only two minor ampullate fibres (diameter

1.018 ± 0.016 µm). Gumfoot threads (Fig. 2E) with six fibres are composed of two minor ampullate (diameter 0.861 ± 0.029 µm), two major ampullate (diameter 0.321 ± 0.044 µm), and aciniform fibres (diameter 0.175 ± 0.030 µm), whereas the eight-fibre gumfoot threads include two additional major ampullate fibres. Both the major and minor ampullate fibres within gumfoot and four-fibre dragline threads exhibited smaller diameters than those observed in two-fibre dragline and bridging line bundles, suggesting that fibre size may be modulated according to functional or spinning conditions. For comparison, scanning electron micrographs of forcibly spun PMS thread and aciniform fibre, which do not reflect natural spinning conditions, are provided in the SI (Fig. S13).

We further investigated the effect of partial stretching on the structure of the fibre bundles. The N4 drop-down dragline samples and gumfoot threads were subjected to strains below their respective breaking points: dragline samples were stretched to 0.1 mm mm^{-1}, while gumfoot threads were stretched to 0.3 and 0.4 mm mm^{-1}. Across the two strained N4 dragline samples examined under the scanning electron microscope, deformation of the medium-sized fibres was observed in only one sample. In this sample, several fibres transitioned from a circular to a flattened or constricted cross-section (Fig. 3A and B), suggesting that the fibres experienced lateral compressive forces in addition to axial tension. The other N4 sample did not show comparable deformation. Instead, it exhibited shallow, scratch-like surface features, while the second sample showed a thin coating that caused several fibres to adhere closely to one another. Both observations are shown in the SI (Fig. S12). The scratch-like patterns are interpreted as local surface defects. In the coated sample, fracture appears to initiate at regions where fibres adhere to one another and intersect with surface scratches, which differs from the first sample, where failure was initiated by the early fracture of thinner fibres.

Under 0.3 mm mm^{-1} strain, six fibres were observed in gumfoot threads, with three distinguishable fibre types (Fig. 3C–F): two large, two medium, and two small fibres, corresponding to minor ampullate, major ampullate and aciniform silk,
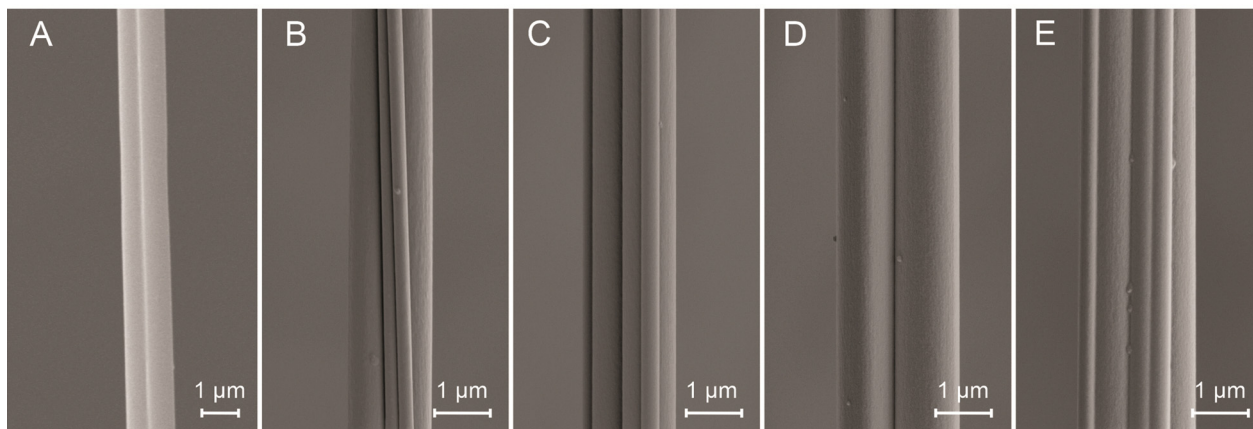

Fig. 2 Scanning electron micrographs of *Pholcus phalangioides* silk bundles naturally spun in different behavioural contexts. (A) Two-fibre drop-down dragline (N2), (B) four-fibre drop-down dragline (N4), (C) walking dragline, (D) bridging line, and (E) gumfoot thread.
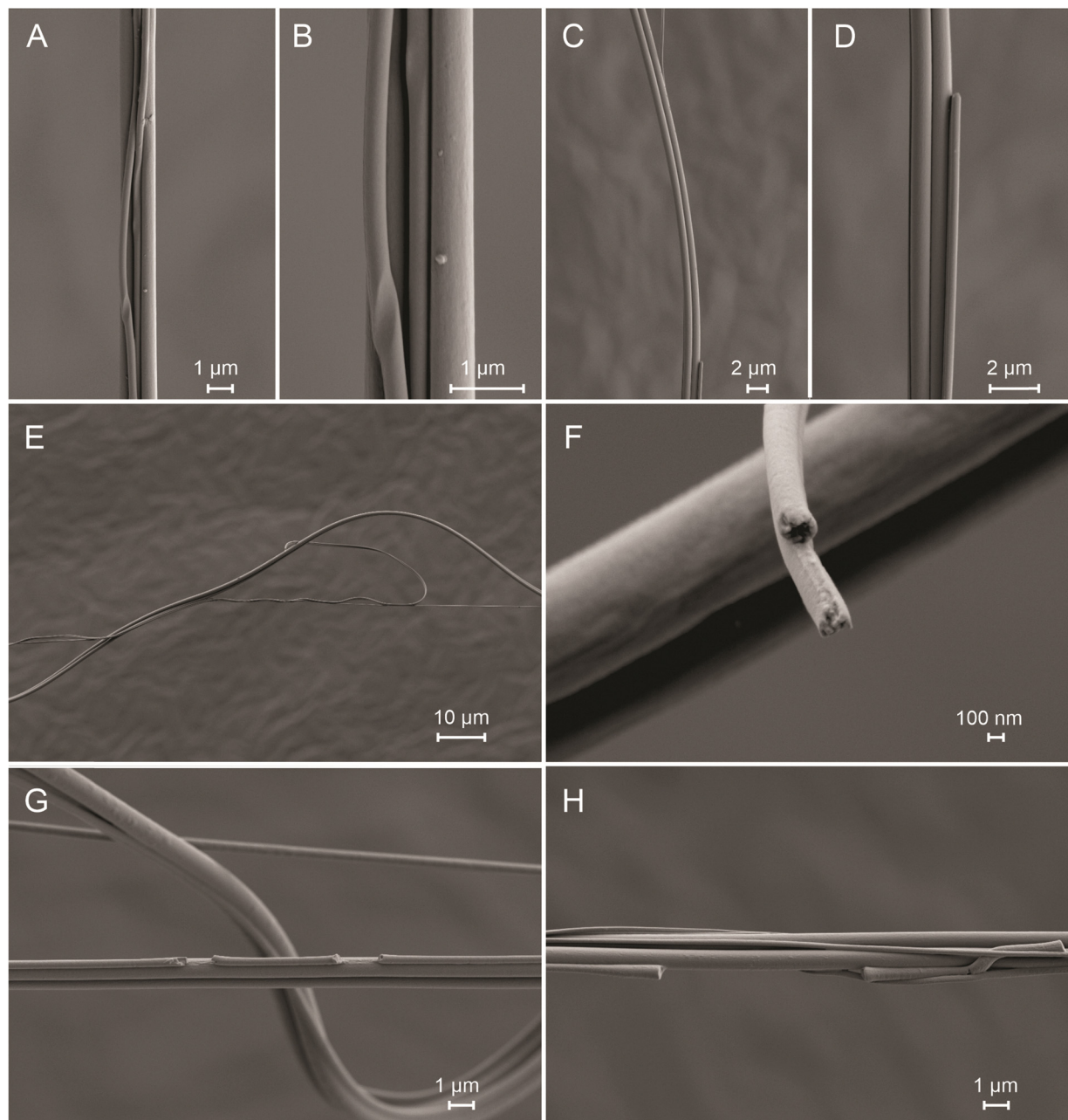
Fig. 3 Scanning electron micrographs of naturally spun *Pholcus phalangioides* silk bundles subjected to tensile stretching at different strain levels: (A) and (B) N4 drop-down dragline after 10% mm mm^{-1} strain, (C)–(F) gumfoot thread after 30% mm mm^{-1} strain, and (G) and (H) gumfoot thread after 40% mm mm^{-1} strain.

respectively. The images show that the major ampullate silk fibres had broken, while the minor ampullate and aciniform silk fibres remained intact (Fig. 3H). In some regions of the bundle, all fibre types were separated (Fig. 3E). The broken major ampullate fibres had a diameter of approximately 200 nm after failure. A similar pattern was observed in gumfoot threads containing more than six fibres under 0.4 mm mm^{-1} strain (Fig. 3G and H), the medium-sized fibres consistently broke first under tensile load. Notably, fibre fracture did not occur at a single location; instead, partial breaks appeared along the fibre length, with some segments remaining intact while others failed,

indicating that rupture occurs progressively rather than instantaneously along the bundle.

Morphology of *Nesticus cellulanus* silk threads

In *N. cellulanus*, we observed a uniform bundle composition across the bundle length, parallel fibre direction, and no particular roughness or any other topological features of the bundle. The drop-down dragline of *N. cellulanus* exhibits similarities to that of *P. phalangioides*, with spiders producing both two- and four-fibre draglines. N2 draglines (Fig. 4A) consisted of two fibres (diameter 1.031 $\pm$ 0.59 µm), while N4 draglines
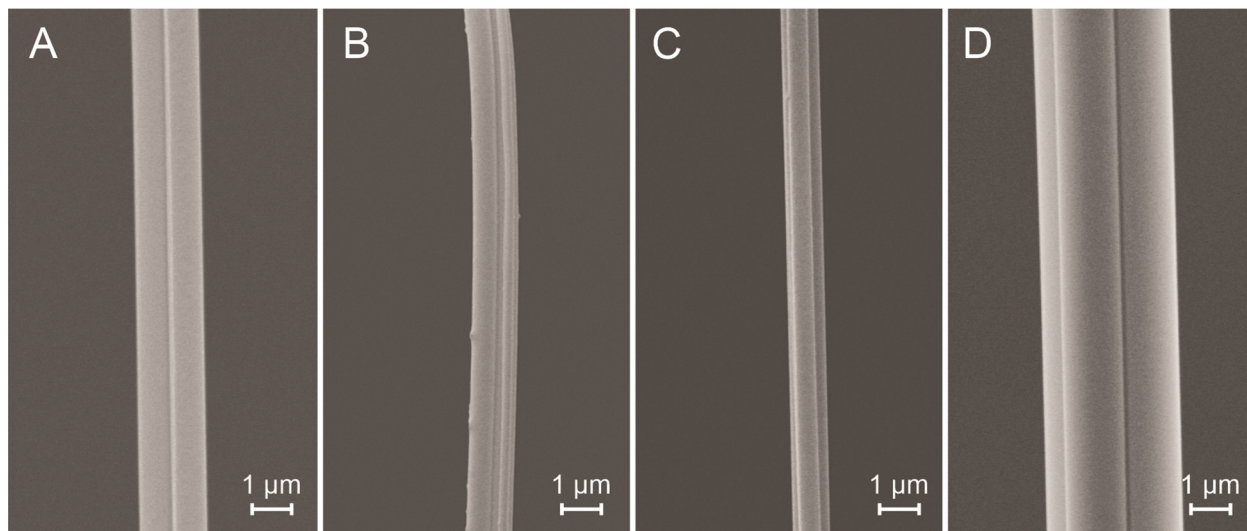
Fig. 4 Scanning electron micrographs of naturally spun *Nesticus cellulanus* silk bundles naturally spun in different behavioural contexts. (A) Two-fibre drop-down dragline (N2), (B) four-fibre drop-down dragline (N4), (C) walking dragline and (D) gumfoot thread.

(Fig. 4B) were composed of two medium fibres (diameter 0.665 ± 0.02 μm) and two smaller fibres (diameter 0.268 ± 0.02 μm), probably corresponding to major ampullate and minor ampullate silk, respectively (as in this species, in contrast to *P. phalangioides*, the major ampullate gland spigots have a larger diameter than the minor ampullate gland spigots). Walking draglines (Fig. 4C) were composed of two large fibres (diameter 1.062 ± 0.03 μm) and two medium fibres (diameter 0.603 ± 0.02 μm). The gumfoot threads of *N. cellulanus* (Fig. 4D) contained a pair of large fibres (diameter 1.686 ± 0.03 μm) and a pair of slightly smaller fibres (diameter 1.351 ± 0.02 μm). We note that different samples selected for SEM were from different spider individuals of different sizes, explaining some of the reported size variation of the major ampullate fibres.

Mechanical properties of *Pholcus phalangioides* silk

Stress–strain curves of both single silk and mixed bundles generally exhibited shapes characteristic of spider silk, with a short elastic phase, followed by a switch in stiffness, sometimes followed by a phase of strain-hardening (Fig. 5). In the case of multi-fibre bundles, force dips indicating internal single-fibre fractures were minimal and expressed multi-peak fractures were rare. Mechanical properties differed between different silk types and bundle configurations as follows. For stress at break (Fig. 6A) there was a significant difference only between bridging lines and pure aciniform silk (Fig. 6A). For strain at break (Fig. 6B), gumfoot threads, aciniform silk, and PMS bundles were significantly different from walking draglines and N2 drop-down draglines. On average, gumfoot threads, aciniform silk, and PMS bundles
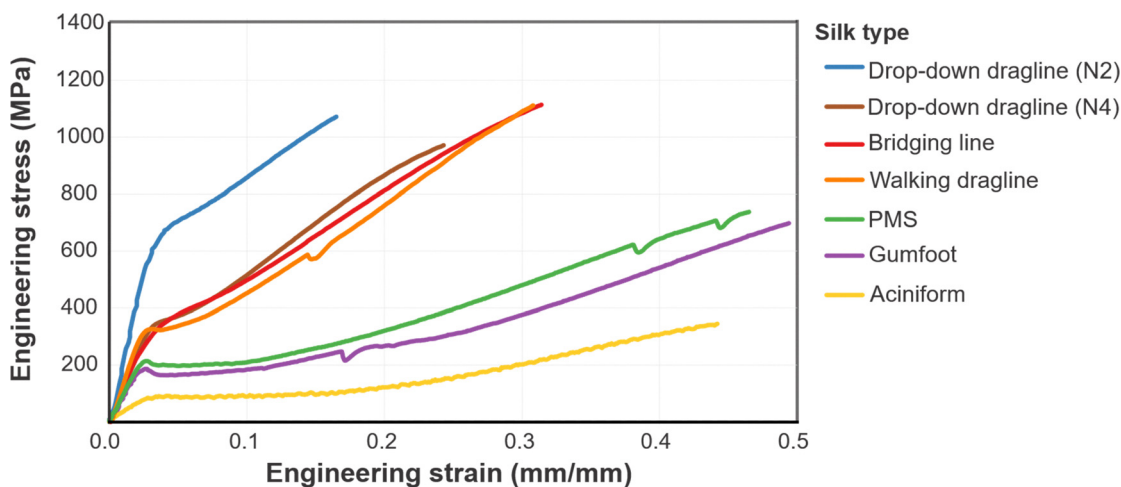

Fig. 5 Comparative stress−strain curves of naturally spun *Pholcus phalangioides* silk bundles (N2 two-fibre dragline, N4 four-fibre dragline, walking dragline, bridging line, and gumfoot thread) and forcibly silked samples (single aciniform fibre and posterior median spinneret fibre bundle, PMS).

could be elongated more than drop-down and walking draglines, whereas walking draglines could be stretched more than N2 drop-down draglines. Yield stress (Fig. 6C) was highest in N2 drop-down draglines (*i.e.*, assumed to be pure major or minor ampullate silk)

and lowest in pure aciniform silk, indicating that N2 draglines can resist higher forces before deforming irreversibly. The highest load at break was observed in bridging line threads, which are composed of two fast-spun minor ampullate fibres (Fig. 6D).
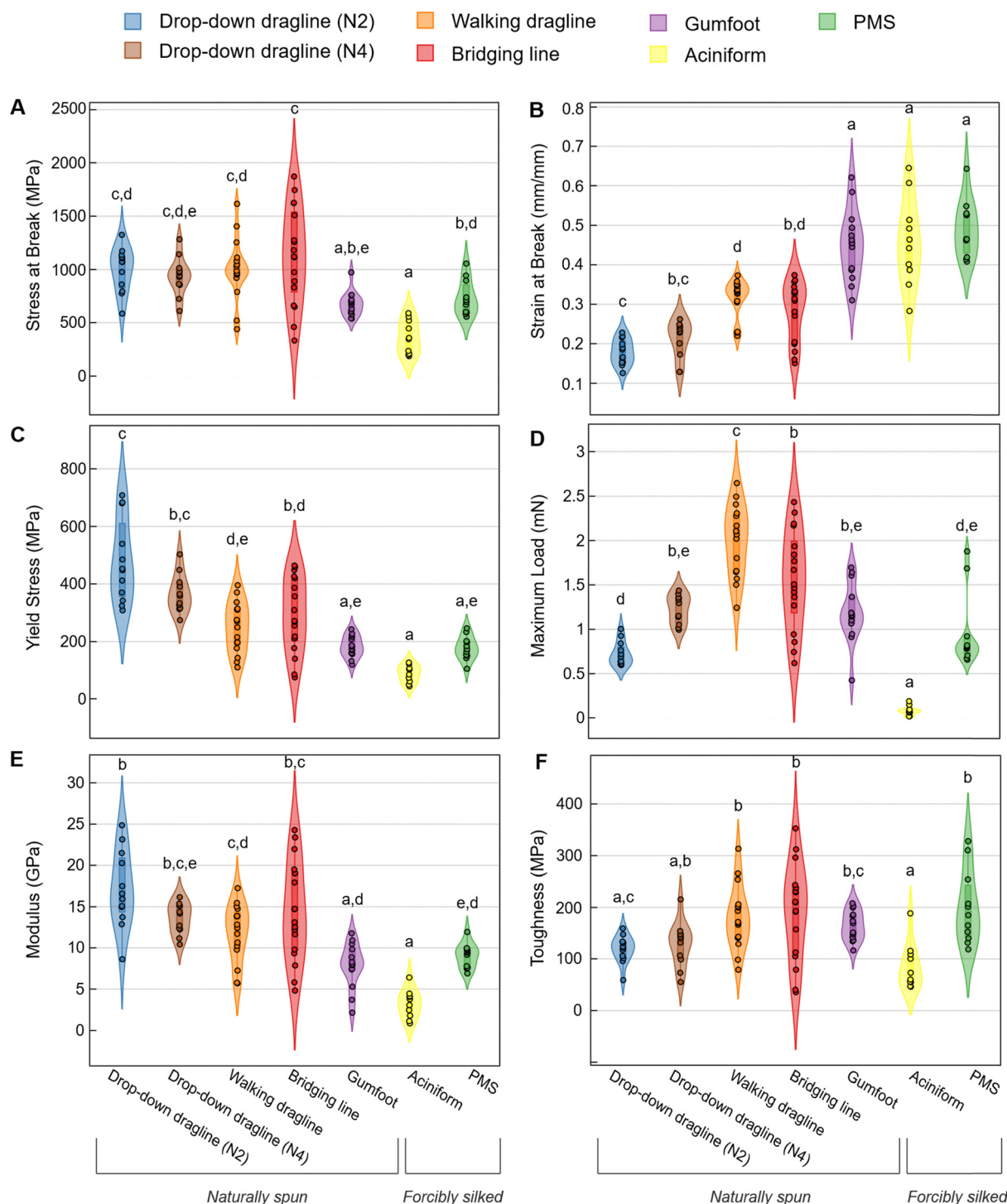

Fig. 6 Violin plots showing the distribution of tensile property data for each sample type from *Pholcus phalangioides*. Different letters above each plot indicate significant differences between group means (Tukey test, $\alpha = 0.05$). Groups sharing no letters in common are significantly different. Raw data and detailed sample information are provided in the SI. (A) Ultimate tensile strength (engineering stress at break). (B) Extensibility (engineering strain at break). (C) Yield stress (engineering stress at yield, *i.e.* maximum stress under the elastic regime). (D) Maximum load (tensile load force at break). (E) Young's modulus (indicator of stiffness). (F) Toughness (maximum energy absorbed before fracture).

Table 1 Mechanical properties of *Pholcus phalangioides* and *Nesticus cellulanus* silk threads. The numbers are given as mean ± standard deviation

Species	Silk Type	Sample size	Sample cross-section area (μm²)	Maximum load (mN)	Toughness (MPa)	Stress at break (MPa)	Strain at break (mm mm⁻¹)	Young's Modulus (GPa)	Yielding stress (MPa)	Yielding strain (mm mm⁻¹)
Pholcus phalangioides	Drop-down dragline (N2)	12	0.76 ± 0.23	0.72 ± 0.14	119.18 ± 26.50	998.32 ± 207.23	0.18 ± 0.03	17.10 ± 4.65	479.61 ± 144.28	0.027 ± 0.004
	Drop-down dragline (N4)	11	1.34 ± 0.22	1.23 ± 0.16	128.65 ± 43.89	937.43 ± 183.16	0.21 ± 0.05	13.57 ± 1.88	366.92 ± 66.48	0.027 ± 0.003
	Walking dragline (N6)	16	2.12 ± 0.57	2.00 ± 0.40	179.68 ± 61.42	1001.43 ± 286.30	0.32 ± 0.05	11.90 ± 3.45	250.20 ± 87.17	0.021 ± 0.004
	Bridging line (N2)	17	1.51 ± 0.51	1.56 ± 0.56	190.55 ± 91.88	1123.72 ± 454.36	0.28 ± 0.08	14.28 ± 5.96	292.54 ± 129.96	0.021 ± 0.004
	Gumfoot thread	14	1.77 ± 0.43	1.18 ± 0.33	164.54 ± 28.71	674.58 ± 112.96	0.45 ± 0.09	7.86 ± 2.68	182.56 ± 36.85	0.026 ± 0.008
	PMS thread	11	1.29 ± 0.32	0.96 ± 0.42	199.55 ± 70.87	731.05 ± 164.33	0.49 ± 0.07	9.03 ± 1.47	177.67 ± 41.09	0.020 ± 0.002
	Aciniform	10	0.24 ± 0.16	0.08 ± 0.05	84.96 ± 44.68	364.68 ± 155.36	0.46 ± 0.11	3.21 ± 1.70	87.39 ± 29.71	0.029 ± 0.008
Nesticus cellulanus	Drop-down dragline (N2)	7	0.55 ± 0.05	0.48 ± 0.13	130.93 ± 64.21	891.62 ± 259.08	0.22 ± 0.05	12.46 ± 2.48	360.47 ± 99.37	0.029 ± 0.004
	Drop-down dragline (N4)	5	1.44 ± 0.39	1.24 ± 0.15	152.19 ± 58.75	886.31 ± 161.12	0.26 ± 0.07	11.77 ± 0.94	334.30 ± 65.75	0.029 ± 0.006
	Walking dragline	10	1.45 ± 1.07	0.90 ± 0.20	134.72 ± 48.95	726.97 ± 200.06	0.31 ± 0.08	10.01 ± 3.11	212.69 ± 84.69	0.022 ± 0.005
	Gumfoot thread	10	3.05 ± 1.86	2.32 ± 1.95	178.88 ± 111.54	804.34 ± 446.12	0.37 ± 0.14	11.05 ± 4.19	225.76 ± 102.00	0.021 ± 0.003

The modulus of N2 draglines was significantly higher than that of aciniform silk (Fig. 6E), consistent with the observed differences in yield stress. As shown in Table 1, the toughness of gumfoot threads was lower than that of walking draglines and bridging lines, whereas PMS threads exhibited the highest toughness among all silk types. Young's modulus values of gumfoot threads and PMS threads were relatively low, exceedingly only those of aciniform fibres, while N2 draglines showed the highest modulus. Finally, the toughness of naturally collected walking draglines, bridging lines, and manually collected PMS threads was significantly greater than that of aciniform silk (Fig. 6F), reflecting their greater ability to absorb energy before failure.

Mechanical properties of silk threads in *Nesticus cellulanus*

Drop-down draglines from *Nesticus cellulanus* could be classified into two types, consisting of either two (N2) or four (N4) fibres. As shown in Fig. 7, N2 and N4 drop-down draglines exhibited comparable tensile behaviour. Walking draglines, by contrast, showed the lowest yield stress and stress at break, whereas the strain at break did not differ substantially among the tested samples.

As shown in Fig. 8, no significant differences were observed among the silk types for stress at break (Fig. 8A), modulus (Fig. 8E), or toughness (Fig. 8F). However, strain at break (Fig. 8B) and maximum load (Fig. 8D) were significantly higher in gumfoot threads compared to N2 drop-down draglines. For yield stress (Fig. 8C), N2 drop-down draglines differed significantly from both gumfoot threads and walking draglines, whereas gumfoot and walking draglines did not differ from each other.

Analysis of silk bundle strength in *P. phalangioides*

The strength distributions of all *P. phalangioides* silk bundle types were in agreement with the two-parameter Weibull distribution, confirming that failure follows the weakest-link principle, characteristic of fibrous materials. Both linear regression and maximum likelihood estimation methods yielded compatible results for parameter determination. The manually collected posterior median spinneret bundles exhibited the weakest correlation with the Weibull model ($R^2 = 0.839$), whilst all other thread types showed strong adherence to the theoretical distribution ($R^2 > 0.857$). All found distributions showed p-values higher than $\alpha = 0.05$, confirming the goodness of fits.

The Weibull analysis revealed considerable variation in mechanical reliability across silk bundle types. Results are presented in Table 2, while the Weibull plots are illustrated in Fig. 9A. Further details on the analysis are reported in the SI. Bridging lines demonstrated the highest characteristic strength ($\sigma_0 = 1280.4$ MPa), but exhibited the greatest variability, with a shape parameter of $m = 2.39$, indicating the least repeatable strength values. Conversely, gumfoot bundles displayed the most consistent mechanical behaviour, $m = 6.71$, despite having the lowest characteristic strength ($\sigma_0 = 721.8$ MPa).

Analysis of the size effect parameter ν revealed that four of the six bundle types exhibited considerable geometrical scaling effects. The drop-down draglines and bridging lines demonstrated ν values ranging from 1.89 to 4.92, exceeding the
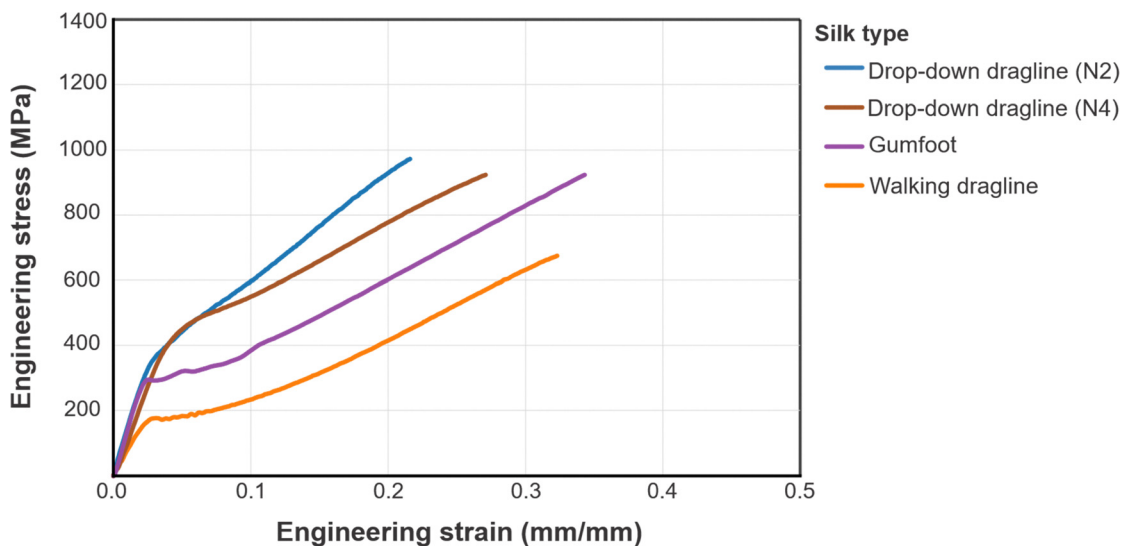
Fig. 7 Comparative stress–strain curves of naturally spun two-fibre dragline, four-fibre dragline, walking dragline, and gumfoot thread from *Nesticus cellulanus*.

normally expected of 0–1.[36–40] When $v > 1$, the material exhibits enhanced size effects beyond those predicted by classical linear elastic fracture mechanics, indicating that effective flaw size decreases more rapidly with specimen dimensions than geometric similarity would predict. This result is not explainable by the inclusion of bundle effects, as the inclusion of non-load bearing fibres should cause a decrease of the scale effect, and not an increase. Indeed, this is the behaviour observed in gumfoot threads. The PMS fibre bundles, the gumfoot threads, and the aciniform silk fibres exhibited non-significant scaling relationships.

Fracture mechanics analysis for *P. phalangioides*

Six of the seven thread types demonstrated statistically significant correlations between strength and the square root of the modulus-to-diameter ratio ($\sqrt{(E/d)}$), as predicted by Griffith's criterion for elastic fracture (Table 3). The strength of these correlations varied considerably across silk types, with bridging lines and walking draglines showing the strongest adherence to the energy criterion ($R^2 = 0.874$ and $R^2 = 0.832$, respectively). Drop-down draglines exhibited robust correlations for both two-fibre ($R^2 = 0.801$, $p = 8.41 \times 10^{-5}$) and four-fibre configurations ($R^2 = 0.520$, $p = 0.012$). The relationships are illustrated in Fig. 9B.

In contrast, posterior median spinneret fibre bundles, aciniform silk fibres, and gumfoot threads showed weaker correlations with the Griffith relationship, with gumfoot threads failing to achieve statistical significance ($p = 0.071$). This deviation suggests that these thread types may not follow classical linear elastic fracture mechanics, potentially due to different internal load-bearing mechanisms or the presence of systematic errors in cross-sectional area measurements arising from non-cylindrical fibre geometry, surface coatings, or, in the case of aciniform fibres, the low values of diameters and Young's moduli.

When correlations were analysed using the simplified relationship $\sigma \propto 1/\sqrt{d}$ (excluding the modulus term), all silk types exhibited reduced coefficients of determination and decreased

statistical significance. This reduction in correlation strength, particularly evident in drop-down draglines, where R^2 decreased from 0.801 to 0.670 for two-fibre bundles, underscores the critical importance of Young's modulus variability in governing silk bundle strength. Further details on the analysis are reported in the SI.

These results indicate that, despite their nonlinear stress–strain behaviour, *P. phalangioides* silk bundles fundamentally adhere to classical fracture mechanics principles. However, the substantial variation in Young's moduli within individual bundle types cannot be adequately represented by average values alone. Each bundle appears to be individually tuned during the spinning process, suggesting that spiders can modulate silk stiffness to achieve specific mechanical targets rather than maintaining consistent material properties.

Statistical and fracture analysis for *N. cellulanus*

Due to limited variation in bundle cross-sectional areas, the fewer produced bundle silk types, and the smaller sample sizes, the statistical and fracture analysis for *N. cellulanus* lead to less significant results. The results are provided in the SI.

The Weibull analysis for *N. cellulanus* confirmed that all four bundle types followed the weakest-link failure principle. Gumfoot bundles exhibited the greatest variability in strength values. The fracture mechanics analysis revealed that *N. cellulanus* bundles also demonstrated higher strength correlations when Young's modulus variation was incorporated into strength predictions. Two-fibre drop-down draglines and walking draglines showed strong adherence to Griffith's criterion using the $\sqrt{E/d}$ relationship, with substantially reduced correlations when modulus variation was ignored. Consistent with *P. phalangioides*, gumfoot bundles showed no meaningful correlation between strength and cross-sectional area, suggesting the presence of primary load-bearing fibres with minimal contribution from additional bundle components.
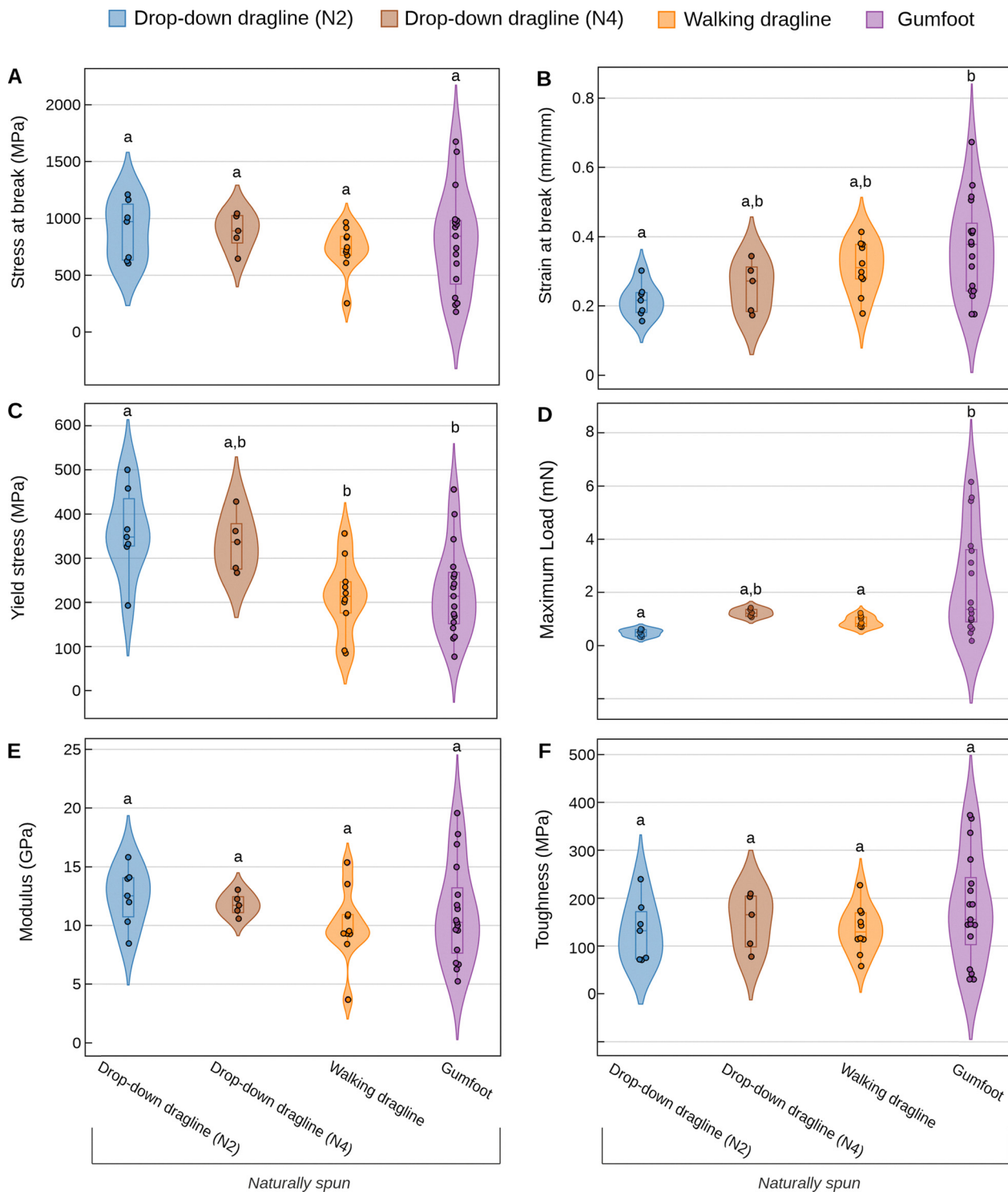
Fig. 8 Violin plots showing the distribution of tensile property data for each sample type from *Nesticus cellulanus*. Different letters above each plot indicate significant differences between group means (Tukey test, $\alpha = 0.05$). Groups sharing no letters in common are significantly different. (A) Ultimate tensile strength (engineering stress at break). (B) Extensibility (engineering strain at break). (C) Yield stress (engineering stress at yield, *i.e.* maximum stress under the elastic regime). (D) Maximum load (tensile load force at break). (E) Young's modulus (indicator of stiffness). (F) Toughness (maximum energy absorbed before fracture).

Finite element modelling of bundle mechanics

Finite element analysis confirmed that contact scenarios between fibres within bundles do not significantly influence mechanical behaviour during the elastic loading phase. Results are presented in the SI. Models comparing separated fibres, fibres in contact, and completely fused four-fibre configurations

Table 2 Results of the two-parameter Weibull analysis conducted on each silk type for *P. phalangioides,* and the scale parameter *v* found when studying the proportionality between strength and cross-section according to the modified Weibull distribution, with asterisks between brackets indicating its significance

Silk type	Sample size	σ [MPa]	$\Delta\sigma$ [MPa]	CV	m	σ_0 [MPa]	p-value	R^2	v
Drop-down dragline (N2)	12	998.3	198.4	0.199	4.86	1088.6	0.75	0.962	2.999 (**)
Drop-down dragline (N4)	11	937.4	174.6	0.186	5.44	1014.2	0.76	0.962	4.92 (**)
Walking dragline	16	1001.4	277.2	0.277	3.41	1121.9	0.40	0.909	3.117 (**)
Bridging line	17	1123.7	440.8	0.392	2.39	1280.4	0.99	0.987	1.789 (**)
PMS	11	731.0	156.7	0.214	4.83	798.0	0.52	0.839	−0.41 (ns)
Gumfoot	14	674.6	108.8	0.161	6.71	721.8	0.74	0.857	0.54 (ns)
Aciniform	10	364.7	147.4	0.404	2.36	417.2	0.88	0.895	0.44 (ns)

all yielded identical load-displacement responses in the linear elastic region. The calculated loads matched those predicted by simple linear superposition, validating the applicability of classical elasticity theory to multi-fibre silk bundles under small deformations. However, simulations of partially fractured bundles for an identical value of externally applied displacement revealed that contact between the fibres leads to the development of high, localised stress concentrations, of intensity depending from the considered geometry but always higher than the value found at equilibrium for an intact bundle. These stresses accumulated at the interfaces between broken and intact fibres, propagating to neighbouring fibres and surpassing the critical stress of all fibres in the bundle, leading to catastrophic failure (Fig. 10). This result was found for every possible Young's modulus, strain at break and stress combination in the range of the mechanical properties found in this study for load bearing fibres of *P. phalangioides, i.e.* major ampullate and minor ampullate fibres. This stress redistribution mechanism explains the absence of multiple prominent peaks in the experimental load-elongation curves, confirming that bundle failure occurs as a single avalanche event rather than through sequential individual fibre failures, except for thin fibres that contribute only little to the bundle's load bearing capacity (see results of scanning electron microscopy of strained fibres and Fig. 3, and little dips in the stress–strain curves of the gumfoot and PMS thread sample in Fig. 5). The models demonstrated that, when fibres are clamped at both ends and loaded in parallel, contact between fibres does not influence elastic behaviour, and all fibres behave as independent media with uniform distributed strain. These results were obtained considering a Poisson's ratio of 0.3, and are not affected by the transverse strains. The modelling results support the experimental observation that silk bundles behave mechanically as equivalent single fibres with cross-sections equal to the sum of their constituent fibres. This behaviour validates the use of the Weibull distribution analysis for bundle strength characterisation and confirms that the observed strength-geometry correlations reflect fundamental material properties rather than inter-fibre interactions while all fibres are intact and stress distribution is homogeneous.

Discussion

Behavioural context and the overlooked complexity of multi-fibre silk bundles

Spider silk research has traditionally focused on the mechanical properties of single fibres and their relationship to molecular structure,[3,15] whilst the mechanical behaviour of multi-fibre bundles has received far less attention. Most studies have examined forcibly silked fibres from immobilised spiders,[15,42–46] thereby excluding the behavioural fibre combinations that occur during spinning. Although cribellate capture threads represent one well studied example of a multi-fibre composite that combines axial fibres, reserve warps and nanofibres into an adhesive and highly extensible structure,[18] their architecture differs fundamentally from the straight, parallel fibre bundles investigated here. In cribellate threads, most components are highly coiled or looped, producing tensile behaviour that is dominated by uncoiling rather than by load sharing among parallel fibres.[16,18] In contrast, dragline, bridging and gumfoot threads in *Pholcus phalangioides* and *Nesticus cellulanus* consist of fibres that run mostly in parallel, making them well suited for testing how spiders combine silk types to create mechanically integrated load bearing bundles. We addressed this gap by examining naturally spun silk bundles in these two non-orb weaving spiders, allowing us to assess how fibre composition, behavioural context and post spinning organisation together influence mechanical performance.

Our study reveals that mechanical properties of *P. phalangioides* bundles violate predictions from composite mechanics. Bridging lines (two minor ampullate fibres) bore on average 1.3 times higher maximum loads than gumfoot threads, despite the latter containing six to eight fibres, including two minor ampullate fibres plus additional silk types, and a larger overall cross-section. Under Hooke's law for parallel clamped fibres, gumfoot load should equal or exceed bridging line load, and the minor ampullate contribution alone should match bridging lines, with additional fibres only increasing the total. The difference found is not justifiable by the smaller fibre cross-sections found in minor ampullate fibres included in gumfoot threads compared to ones forming bridging line threads: gumfoot threads still show a higher average cross-section, due to the higher number of included fibres. This indicates that "minor ampullate" fibres differ fundamentally between thread types, depending on spinning conditions. Similarly, gumfoot threads exhibited Young's modulus 2.2 times lower than N2 draglines, despite both containing primarily ampullate fibres. This variation is not explainable by the sole inclusion of aciniform silk fibres, due to the relatively low contribution expected from them when considering their small cross-sectional area, $\leqslant 15\%$ of the area of the ampullate fibres.

The distinct mechanical behaviour of gumfoot threads and bridging lines can be linked to their spinning behaviours.
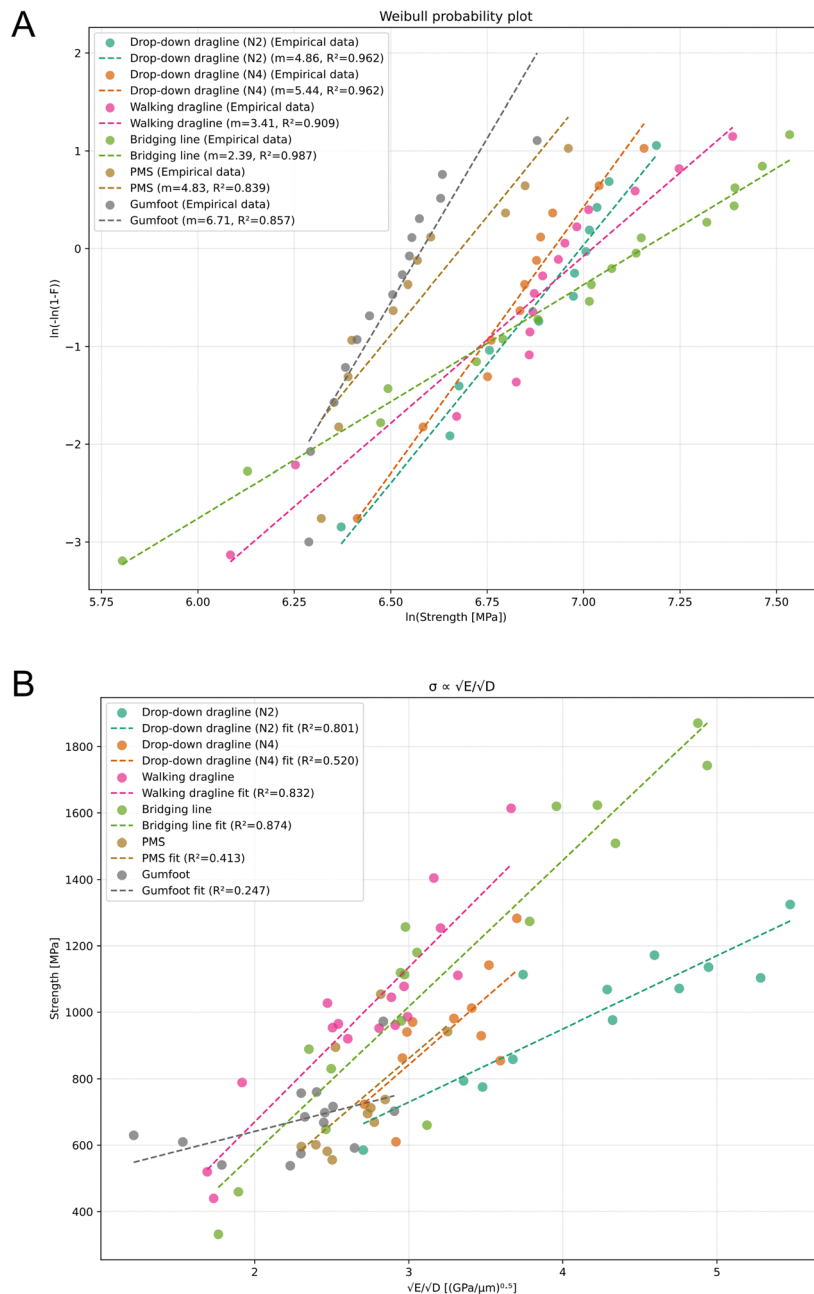
Fig. 9 Weibull and fracture analysis on the bundles spun by *P. phalangioides*. (A) Weibull plot, showing the logarithm of the strength against the logarithm of the negative logarithm of the survival probability ($1 - P$). Linear regression results are reported as dashed lines for each thread type. All thread types agree with the weakest-chain link distribution. (B) Fracture mechanics relationships for *P. phalangioides* threads, showing the squared ratio of the Young's modulus and the bundle equivalent diameter against the strength. The plot demonstrates the correlation between stress at break and the square root of the Young's modulus-to-diameter ratio for each thread type. Linear regression fits (dashed lines) validate the prediction illustrated in ref. 41, as predicted by Griffith's criterion. Aciniform silk fibres are excluded here due to scale differences (see SI).

Gumfoot construction in *P. phalangioides* is highly stereotyped: the spider moves slowly toward the substrate, attaches the line, and then ascends while laying and tensioning silk to store elastic energy.[28] This behavioural consistency likely contributes to the low variation in gumfoot thread properties, regardless of fibre number. In contrast, bridging line construction, although also stereotyped, involves alternating leg movements that produce variable reeling speeds and bundle strengths,[27] as confirmed by the Weibull analysis. These different spinning behaviours explain the mechanical differences: gumfoot threads are deposited under tension within the web, which may prestrain the fibres and affect their extensibility and toughness,[47,48] whereas the higher speed spinning of draglines and bridging lines can lead to stiffer fibres, adapted to load-bearing functions.[27] Furthermore, there is also a difference between bridging lines and drop-down draglines, as the latter are produced *via* whole body descent.

Table 3 Fracture mechanics analysis correlating bundle equivalent diameter with tensile strength for *P. phalangioides*, using the relationships $\sigma \propto \sqrt{E}/\sqrt{d}$ and $\sigma \propto 1/\sqrt{d}$ for each silk bundle type, presenting coefficients of determination (R^2) and statistical significance (*p*-values)

| Silk type	d [μm]	E [GPa]	σ vs. $\sqrt{E/d}$ *p* value	σ vs. $\sqrt{E/d}$ R^2	σ vs. $\sqrt{1/d}$ *p* value	σ vs. $\sqrt{1/d}$ R^2
Drop-down dragline (N2)	0.973	17.098	8.41×10^{-5}	0.801	0.001	0.670
Drop-down dragline (N4)	1.302	13.575	0.012	0.520	0.006	0.586
Walking dragline	1.628	11.907	8.72×10^{-7}	0.832	4.17×10^{-4}	0.601
Bridging line	1.366	14.281	3.93×10^{-8}	0.874	0.003	0.462
PMS	1.272	9.035	0.033	0.413	0.810	0.007
Gumfoot	1.487	7.860	0.071	0.247	0.626	0.020
Aciniform	0.527	3.212	0.031	0.461	0.930	0.001
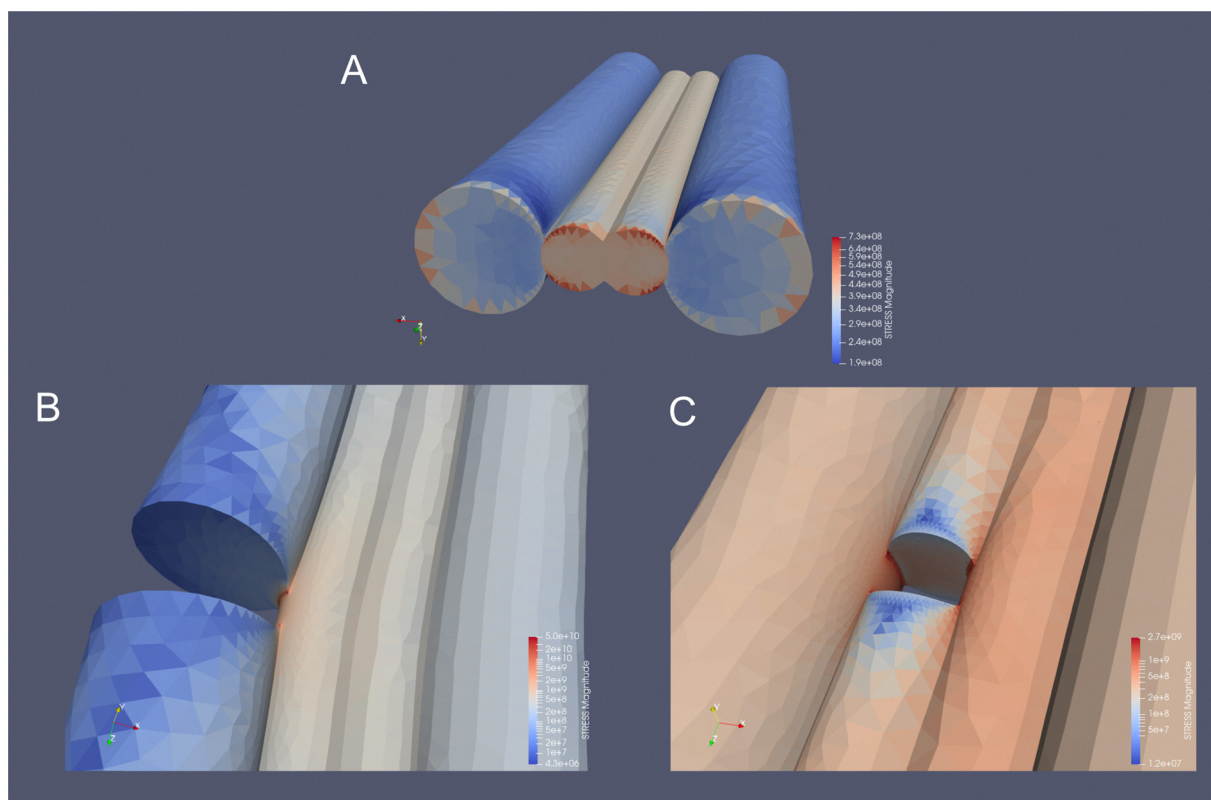
Fig. 10 Stress distributions in fibre bundles in intact and partially fractured scenarios. The outer fibres have an area four times larger than the internal ones. (A) Intact bundle. For every geometrical configuration, the stress is homogeneously distributed outside of the clamped region. The ratio between the stresses in the different fibres reflect the ratios between the different Young's moduli. (B) Failure of a large fibre. Stresses concentrate at the interface with neighbouring fibres for all contact scenarios. Stresses at the interface between the neighbouring fibre and the fracture are ⪅100 times higher than in figure A. (C) Failure of a small fibre. Here, stress concentrations lead to stresses ⪅4 higher than in figure A. In both figures (B) and (C), stress concentration would lead to an avalanche that leads to immediate fracture of the entire bundle. Similar results are found for all geometrical configurations considered.

This finding demonstrates that silk type classification by gland origin inadequately predicts mechanical behaviour, consistent with Blackledge *et al.* (2005), who demonstrated that capture-thread performance in cobweb spiders depends on more than fibre composition.[27,47,49,50] Instead, the same gland can produce fibres with differing load-bearing capacity depending on the spinning context.[51]

Influence of bundle architecture and morphology

Morphological analysis revealed distinct fibre arrangements across behaviours in *P. phalangioides*: producing two fibres for drop-down draglines and bridging lines, yet incorporating more complex arrangements of four fibres for certain draglines, six fibres for walking draglines, and six to eight fibres for gumfoot threads.[24] While the glandular origin of each fibre type observed in the bundles was not directly observed, we could infer the silk types from the systematic differences in fibre diameters and previously reported gland activation patterns during different spinning behaviours.[27,52] The two-fibre drop-down draglines and bridging lines are consistent with production from a single silk gland type of major ampullate and minor ampullate silk, respectively.[27] In contrast, the more

complex bundles contain fibres of multiple diameter classes, which is consistent with the involvement of additional silk types, such as aciniform silk, as reported previously for this species.

Our morphological observations also challenge the prevalent assumption that draglines are solely made of major ampullate silk.[15,48] Instead, multiple fibre types were incorporated across different behavioural contexts. Silks produced during locomotion, web construction, or prey capture exhibited distinct stress–strain profiles, indicating behavioural control over fibre composition and spinning conditions.[45,53–57] This is also evident for forcibly silked fibre bundles from the posterior median spinneret, which should exhibit properties dominated by minor ampullate silk, yet their maximum load differed from those of walking draglines, which are spun from the same material and were more similar to gumfoot threads. Whilst previous work demonstrated humidity and reeling speed effects on individual silk fibres,[58–60] our results extend these observations to naturally spun multi-fibre systems, and potentially reveal that spider behaviour can influence the internal structure of the fibres.

Mechanical performance scaling, variability, and fracture behaviour

Our tensile tests show trends in how performances vary between bundles of different sizes. Within dragline types, load scaled predictably: N4 draglines sustained 1.7 times greater loads than N2 draglines, close to the approximate twofold increase. However, Young's modulus decreased from N2 to N4 draglines (from 17.10 to 13.57 GPa), indicating the inclusion of softer silks.

Statistical analysis using the Weibull distribution revealed that multi-fibre bundles showed more reproducible strength than two-fibre threads, with shape parameters in Table 2 ranging from $m = 6.71$ for gumfoot threads to $m = 2.39$ for bridging lines. These values exceed those found in previous spider silk studies, typically ranging from 1.5–3.0,[39] indicating a relatively high repeatability in *P. phalangioides* threads. The advantage of multi-fibre configurations, therefore, lies in more predictable strength rather than enhanced load-bearing capacity, challenging the assumption that spiders use redundancy to enhance mechanical performance. Furthermore, all silk threads agree with Weibull statistics, indicating that the bundles fail catastrophically once a load-bearing fibre fails. It should be noted here that spider silk has a Poisson's ratio usually of 0.3.[29] At high strain, we expect the cross-section restriction to happen asymmetrically, as the constraints given by the surrounding fibres in contact act on the bundle. It is impossible to estimate the effects of this restriction on the fracture behaviour of these bundles without knowing the properties of the individual fibres; however, we can predict that, while the interaction between the fibres holds, the bundle should behave as a single restricting unit, and the contact area between the fibres should increase. If a critical shear stress is reached, the adhesion layer would fail and the two fibres would separate abruptly. We found no clear evidence from our study about which of the two behaviours is more common in the bundles of *P. phalangioides* and *N. cellanus*.

Fracture mechanics analysis revealed correlations between strength and $\sqrt{E/d}$ for all dragline and bridging line bundle types, consistent with material fracture predictions based on a crack of characteristic size *d*. However, these relationships hold only if we consider for each bundle its specific Young's modulus. When scale alone was used as a predictor, or if an average value of Young's modulus was considered for each gland product, the strength correlations failed. This supports the idea that each thread behaves similarly to a single fibre of distinct stiffness and strength, rather than a combination of fibres with pre-determined Young's moduli.

The computational models validated both the Weibull and the fracture analysis. The finite element method showed that, when parallel fibres clamped at both ends are extended, contact between fibres does not influence elastic behaviour, as completely fused fibres had the load response predicted by Hooke's law for separated fibres until the first fracture. After the ultimate strength of any major load-bearing fibre in the bundle is reached, contact between the fibres causes stress concentrations to accumulate on the surviving fibres at the border of the forming crack (Fig. 10), thus leading to a rapid failure propagation throughout the entire bundle structure.

The presence of avalanches is also reinforced by our empirical results and our statistical analysis. Avalanche failure requires that individual fibre strengths be narrowly distributed, something that we cannot directly determine. However, the high Weibull moduli found in this study suggest that this is indeed the case, in particular for gumfoot threads. The FEM model validates the presence of high local stresses for strengths distributed in the found ranges, as already discussed. The application of elastic mechanics, and in ultimate instance of the Fibre Bundle Model presented in the SI, reinforces this by showing how a non-interacting bundle of fibres, lacking the presence of avalanches, would show a different behaviour of the load–displacement curve for these threads. In such a case, well-visible peaks would appear at the moment of fracture of the single fibres forming the bundles. These considerations all indicate the presence of a surface interaction, be it surface friction, local adhesive points, or the presence of chemical interactions between the fibres, mediated or not by the coating surrounding them. Our techniques are not able to discern the exact nature of this interaction, but we know from our results that their strength has to be high enough to sustain the shear stresses caused by the cross-section restriction associated with the non-null Poisson's ratio of spider silk.

We also note here that, while some of the FESEM images reported here show regions where contact between fibres is not complete, these could be artifact of the manipulation that happened on the strained fibres (Fig. 3) and/or the effect of the complete lack of water molecules in the vacuum of the SEM chamber, which is known to cause the presence of deformation and shear stresses in silk.[29] If those regions or non-contact were present in the pristine natural thread, local adhesive points could still mediate the aforementioned load transmission between the different fibres. These local contacts would

themselves be a focal stress accumulation point, changing the behaviour of the predicted avalanches by creating not a continuous fracture front, but one split in two or more parts, in a brick-like fashion. Determining the behaviour of this fracture goes beyond the scope of this study, as it requires a knowledge of the properties of the fibres and their interfaces.[61]

To assess whether this cooperative failure behaviour is unique to spider silk, we conducted tensile tests on artificial polymer bundles composed of nylon and polyethylene fibres (Fig. S10). Unlike natural silk bundles, the synthetic bundles exhibited gradual load reduction and stepwise stress–strain curves as individual fibres fractured independently. Their maximum load could be predicted from cross-sectional area and material modulus, consistent with classical composite mechanics. This contrast indicates that the single-fibre-like behaviour of spider silk bundles during fracture arises from intrinsic inter-fibre coupling, potentially mediated by surface adhesion, residual tension, or protein network rearrangements, highlighting a level of structural integration not achievable in mechanically assembled synthetic fibre bundles.

In particular, spider dragline silk exhibits a pronounced hierarchical organisation, consisting of a core–shell architecture with multiple compositional layers, including an outer lipid coat, glyco layer, skin layer, and distinct core regions. These outer surface layers may enhance the effective contact area and promote adhesive interactions between neighbouring fibres, providing a plausible physical mechanism for strong inter-fibre coupling.[62]

Experimental limitations

Some limitations influence the interpretation of these results, particularly regarding fibre composition. Silk types were inferred from fibre diameters and previous observations of gland activities (see details in ref. 27). However, diameters may vary during spinning processes, as shown for major and minor ampullate silk of *P. phalangioides*.[27,52] Therefore, some N2-draglines may consist of two major ampullate fibres, while others contain two minor ampullate fibres, both of which occur naturally.[27] This likely contributes to the observed variation. Spectroscopic or proteomic analyses could confirm the silk types included in the bundles but require several to hundreds μg of material,[7,63,64] more than a *P. phalangioides* might produce over its lifespan.

Sample size also constrained the analysis. For *N. cellulanus*, fewer individuals and less bundle diversity limited statistical comparisons.[55] Nevertheless, its data remain valuable, as its threads primarily contain major ampullate silk and show less variation in fibre number. Cross-sectional area measurements assumed circular fibre geometry,[29,33,51] which may introduce systematic errors for bundles containing flattened or irregularly shaped fibres.[29,65] However, our diameter measurements, taken at multiple points along each fibre length, showed no significant variation that would indicate strongly elliptical cross-sections. Furthermore, SEM images showing flattened or constricted fibres (*e.g.*, Fig. 3) represent strained conditions after tensile loading rather than the initial fibre geometry used for cross-sectional area calculations. Such errors are likely

greatest in gumfoot threads, where weak correlations between strength and area suggest structural irregularities. In these threads, some fibres are not fully aligned and form small loops or vine-like structures within the bundle (Fig. S11).

Broader implications and perspectives for biomimetic design

The implications of these findings extend beyond spider silk mechanics. The mechanisms underlying material variability control during spinning require elucidation, particularly the relationship between spider behaviour, spinning kinematics, and resulting mechanical properties.[45] *Pholcus phalangioides* appears exceptional in this regard, exhibiting a high degree of variability in silk bundle composition and performance even within the same behavioural context. In contrast, orb-weaving spiders display clearer distinctions between silk types and lower variability within each thread, reflecting more specialised gland functions and spinning behaviours.[11,29,55] Our results from *Nesticus cellulanus*, which is phylogenetically closer to orb weavers, indicate that the parallel bundle architecture and integrated mechanical behaviour observed here are not restricted to *P. phalangioides*. Together, these findings suggest that in some spider lineages, functional diversity in silk threads is achieved primarily through behavioural modulation during spinning rather than through differential use of distinct silk gland products.

Real-time monitoring of spinning conditions,[66] combined with subsequent mechanical testing, could reveal how spiders achieve such precise material control. Improved methods for analysing individual fibres within intact bundles could also resolve current limitations. Advanced spectroscopic methods may reveal whether compositional differences exist between minor ampullate fibres in gumfoot threads and bridging lines. The differences between threads observed in our statistical and fracture analysis should be investigated across additional taxa to determine whether they represent general silk mechanics or species-specific adaptations.[49] Comparative studies incorporating orb-weaving and non-orb-weaving species[16,67] could reveal the evolutionary distribution of this phenomenon and how much these variations are observed in spiders having more than three silk-producing glands. Future biomimetic applications should focus on post-spinning modification techniques[68] that could replicate the material tunability observed in natural silk production.

The integration of empirical data, Weibull statistics,[39] fracture mechanics analysis,[41,69] and finite element modelling provides a coherent framework for understanding silk bundle behaviour. This approach moves beyond simple rule-of-mixtures predictions, showing that each silk bundle behaves as a cohesive material rather than a collection of independent fibres. These insights open new perspectives for understanding natural silk function and guiding biomimetic material design based on adaptive property control instead of static composition optimisation.

Conclusion

This study demonstrates that the tensile properties of spider silk bundles cannot be predicted solely from their constituent

fibre types. In *Pholcus phalangioides* and *Nesticus cellulanus*, bundle morphology and composition varied systematically across behaviours, yet mechanical performance did not scale directly with fibre number or the diversity of included silk types. Two-fibre draglines and bridging lines consistently exhibited the highest yield stress and modulus, reflecting their critical role in weight-bearing and emergency descent, whereas multi-fibre bundles such as gumfoot threads showed greater extensibility and more repeatable yet reduced strength. These results suggest that spiders behaviourally tune the mechanical properties of their threads by fibre extraction and processing dynamics, rather than relying on fixed material compositions.

By integrating tensile testing, scanning electron microscopy, and fracture mechanics analysis, our work provides new insights into the structure–property relationships of mixed-fibre silk bundles. These findings underscore the importance of considering natural spinning behaviours when interpreting spider silk mechanics and open opportunities for biomimetic fibre design strategies that emphasise adaptive property control over static composition.

Author contributions

Conceptualisation: SP, MJ, DL, JOW; methodology: SP, MJ, PH, DL, TI, JOW; validation: SP, TI, DL, JOW; formal analysis: SP, MJ, TI, DL; investigation: SP, MJ, PH, TI, DL; resources: JOW; data curation: SP, TI, DL; writing – original draft: SP, DL; writing – review & editing: SP, DL, JOW; visualization: SP, TI, DL, JOW; supervision: JOW; project administration: JOW; funding acquisition: JOW.

Conflicts of interest

There are no conflicts to declare.

Data availability

The data that support the findings of this study are available in the supplementary information of this article. The supplementary information includes the statistical analysis of the strength of the bundles for both species, including tables and figures; the fracture analysis of the strength of the bundles for both species, including tables and figures; a discussion about the internal characteristic of the bundles and the fibre properties, including Finite Element Method Analysis and Linear Elastic Model analysis; presentation of the artificial polymeric fibre bundle tensile test and sample preparation. See DOI: https://doi.org/10.1039/d5sm01141h.

Acknowledgements

References

1 I. Agnarsson, M. Kuntner and T. A. Blackledge, *PLoS One*, 2010, **5**, e11234.
2 J. Kreuz, P. Michalik and J. Wolff, *J. Morphol.*, 2024, **285**, e21670.
3 L. Römer and T. Scheibel, *Prion*, 2008, **2**, 154–161.
4 Y. Gu, L. Yu, J. Mou, D. Wu, P. Zhou and M. Xu, *e-Polym.*, 2020, **20**, 443–457.
5 Q. Wang, P. McArdle, S. L. Wang, R. L. Wilmington and Z. Xing, *et al.*, *Nat. Commun.*, 2022, **13**, 4329.
6 M. Denny, *J. Exp. Biol.*, 1976, **65**, 483–506.
7 S. Sonavane, S. Hassan, U. Chatterjee, L. Soler and L. Holm, *et al.*, *Sci. Adv.*, 2024, **10**, eadn0597.
8 H. Nakamura, N. Kono, M. Mori, H. Masunaga, K. Numata and K. Arakawa, *Biomacromolecules*, 2023, **24**, 2042–2051.
9 Z. Peng and R. Wen, *Biochimie*, 2025, **230**, 23–32.
10 J. O. Wolff, J. M. Schneider and S. N. Gorb, in *Biotechnology of Silk*, ed T. Asakura and T. Miller, Springer Netherlands, Dordrecht, 2014, pp. 165–177.
11 T. A. Blackledge and C. Y. Hayashi, *J. Exp. Biol.*, 2006, **209**, 2452–2461.
12 W. Tharaka, O. W. Jonas and M. S. Jutta, *J. Arachnol.*, 2025, **52**, 266–273.
13 N. A. H. Abdullah, K. S. K. Ismail, K. H. A. Rahman, J. A. Mohtar and M. M. A. B. Abdullah, *et al.*, *Fibers Polym.*, 2023, **24**, 1029–1038.
14 J. L. Yarger, B. R. Cherry and A. van der Vaart, *Nat. Rev. Mater.*, 2018, **3**, 18008.
15 K. Arakawa, N. Kono, A. D. Malay, A. Tateishi and N. Ifuku, *et al.*, *Sci. Adv.*, 2022, **8**, eabo6043.
16 D. Piorkowski, T. A. Blackledge, C.-P. Liao, A.-C. Joel and M. Weissbach, *et al.*, *J. Exp. Biol.*, 2020, **223**, jeb215269.
17 B. D. Opell and J. E. Bond, *Biol. J. Linn. Soc.*, 2000, **70**, 107–120.
18 D. Liprandi, M. Ramírez, S. Schlüter, L. Baumgart and A. C. Joel, *et al.*, *Interface Focus*, 2024, **14**, 20230071.
19 H. M. Peters, in *Ecophysiology of Spiders*, ed W. Nentwig, Springer Berlin Heidelberg, Berlin, Heidelberg, 1987, pp. 187–202.
20 C. C. F. Grannemann, M. Meyer, M. Reinhardt, M. J. Ramírez, M. E. Herberstein and A.-C. Joel, *Sci. Rep.*, 2019, **9**, 17273.
21 A.-C. Joel, P. Kappel, H. Adamova, W. Baumgartner and I. Scholz, *Arthropod Struct. Dev.*, 2015, **44**, 568–573.
22 W. Eberhard and F. Pereira, *J. Arachnol.*, 1993, **21**, 161–174.
23 S. P. Benjamin and S. Zschokke, *J. Insect Behav.*, 2002, **15**, 791–809.
24 J. O. Wolff, L. J. Ashley, C. Schmitt, C. Heu and D. Denkova, *et al.*, *J. R. Soc., Interface*, 2024, **21**, 20240123.

25 P. Colomban, M. Dinh, A. Tournié and V. Jauzein, *J. Raman Spectrosc.*, 2012, **43**, 1042–1048.

26 J. Li, S. Li, J. Huang, A. Khan and B. An, *et al.*, *Adv. Sci.*, 2021, **9**, 2103965.

27 M. Jani, S. Promnil, P. Heinz, D. Liprandi and J. O. Wolff, *J. Exp. Biol.*, 2025, **228**, jeb250392.

28 H. F. Japyassú and C. R. Macagnan, *Rev. Etol.*, 2004, **6**, 79–94.

29 G. Greco, B. Schmuck, S. K. Jalali, N. M. Pugno and A. Rising, *Biophys. Rev.*, 2023, **4**, 031301.

30 F. Vollrath, B. Madsen and Z. Shao, *Proc. R. Soc. B*, 2001, **268**, 2339–2346.

31 T. A. Blackledge, J. E. Swindeman and C. Y. Hayashi, *J. Exp. Biol.*, 2005, **208**, 1937–1949.

32 G. Greco, M. F. Pantano, B. Mazzolai and N. M. Pugno, *Sci. Rep.*, 2019, **9**, 5776.

33 T. Blackledge, R. Cardullo and C. Hayashi, *Invertebr. Biol.*, 2005, **124**, 165–173.

34 P. Virtanen, R. Gommers, T. E. Oliphant, M. Haberland and T. Reddy, *et al.*, *Nat. Methods*, 2020, **17**, 261–272.

35 L. Kaczmarczyk, Z. Ullah, K. Lewandowski, X. Meng and X. Zhou, *et al.*, *J. Open Source Softw.*, 2020, **5**, 1441.

36 E. Trujillo, M. Moesen, L. Osorio, A. W. Van Vuure, J. Ivens and I. Verpoest, *Composites, Part A*, 2014, **61**, 115–125.

37 K. Naito, *J. Appl. Polym. Sci.*, 2013, **128**, 1185–1192.

38 A. S. Watson and R. L. Smith, *J. Mater. Sci.*, 1985, **20**, 3260–3270.

39 G. Greco and N. M. Pugno, *Molecules*, 2020, **25**, 2938.

40 F. Wang and J. Shao, *Polymers*, 2014, **6**, 3005–3018.

41 D. Porter, J. Guan and F. Vollrath, *Adv. Mater.*, 2013, **25**, 1275–1279.

42 K. Yazawa and U. Sasaki, *Int. J. Biol. Macromol.*, 2021, **168**, 550–557.

43 G. V. Guinea, M. Elices, J. I. Real, S. Gutiérrez and J. Pérez-Rigueiro, *J. Exp. Zool., Part A: Comp. Exp. Biol.*, 2005, **303**, 37–44.

44 G. V. Guinea, M. Elices, J. Pérez-Rigueiro and G. R. Plaza, *J. Exp. Biol.*, 2005, **208**, 25–30.

45 J. Pérez-Rigueiro, M. Elices, G. Plaza, J. Real and G. Guinea, *J. Exp. Biol.*, 2005, **208**, 2633–2639.

46 G. V. Guinea, J. Pérez-Rigueiro, G. R. Plaza and M. Elices, *Biomacromolecules*, 2006, **7**, 2173–2177.

47 T. A. Blackledge, A. P. Summers and C. Y. Hayashi, *Zoology*, 2005, **108**, 41–46.

48 C. Boutry, M. Řezáč and T. A. Blackledge, *PLoS One*, 2011, **6**, e22467.

49 J. O. Wolff, *Evolution*, 2024, **78**, 2032–2038.

50 T. A. Blackledge, *J. Arachnol.*, 2012, **40**, 1–12.

51 C. Boutry and T. A. Blackledge, *Zoology*, 2009, **112**, 451–460.

52 M. Jani, M. Ramírez and J. O. Wolff, *J. Arachnol.*, 2025, **53**(125–133), 129.

53 F. Vollrath and D. P. Knight, *Nature*, 2001, **410**, 541–548.

54 K. Yazawa, A. D. Malay, H. Masunaga, Y. Norma-Rashid and K. Numata, *Commun. Mater.*, 2020, **1**, 10.

55 G. Greco, H. Mirbaha, B. Schmuck, A. Rising and N. M. Pugno, *Sci. Rep.*, 2022, **12**, 3507.

56 R. Young, C. Holland, Z. Shao and F. Vollrath, *MRS Bull.*, 2021, **46**, 915–924.

57 R. Olivé and N. Cohen, *Int. J. Solids Struct.*, 2025, **322**, 113592.

58 N. Du, X. Y. Liu, J. Narayanan, L. Li, M. L. M. Lim and D. Li, *Biophys. J.*, 2006, **91**, 4528–4535.

59 S. Blamires, C.-L. Wu, T. Blackledge and I. M. Tso, *J. R. Soc. Interface*, 2012, **9**, 2479–2487.

60 N. Cohen, M. Levin and C. D. Eisenbach, *Biomacromolecules*, 2021, **22**, 993–1000.

61 L. Brely, F. Bosia and N. M. Pugno, *Front. Mater.*, 2015, **2**, 51.

62 A. Sponner, W. Vater, S. Monajembashi, E. Unger, F. Grosse and K. Weisshart, *PLoS One*, 2007, **2**, e998.

63 T. Pham, T. Chuang, A. Lin, H. Joo and J. Tsai, *et al.*, *Biomacromolecules*, 2014, **15**, 4073–4081.

64 J. R. A. dos Santos-Pinto, H. A. Arcuri, F. G. Esteves, M. S. Palma and G. Lubec, *Sci. Rep.*, 2018, **8**, 14674.

65 G. Greco, J. Francis, T. Arndt, B. Schmuck and F. G. Bäcklund, *et al.*, *Molecules*, 2020, **25**, 3248.

66 J. O. Wolff, *Diversity*, 2020, **12**, 4.

67 T. A. Blackledge and C. Y. Hayashi, *J. Exp. Biol.*, 2006, **209**, 3131–3140.

68 G. Greco, B. Schmuck, F. G. Bäcklund, G. Reiter and A. Rising, *ACS Appl. Polym. Mater.*, 2024, **6**, 14342–14350.

69 P. Poza, J. Pérez-Rigueiro, M. Elices and J. Llorca, *Eng. Fract. Mech.*, 2002, **69**, 1035–1048.